

# Diattenuation of brain tissue explained by finite-difference time-domain simulations

Miriam Menzel<sup>1,2,\*</sup>, Markus Axer<sup>1</sup>, Katrin Amunts<sup>1,3</sup>, Hans De Raedt<sup>4</sup>  
& Kristel Michielsen<sup>5</sup>

In brain tissue, two different types of diattenuation (polarization-dependent attenuation) can be observed: in some brain regions, the light is minimally (maximally) attenuated when it is polarized parallel to the nerve fibers, referred to as  $D^+$  ( $D^-$ ). Here, we demonstrate that diattenuation of type  $D^+$  or  $D^-$  is observed in brain tissue samples from different species and depends on fiber composition and sample age. Using finite-difference time-domain simulations, we show that the observed diattenuation effects are caused by anisotropic absorption (dichroism) and by anisotropic light scattering. Our simulations affirm that regions with out-of-plane fibers only show diattenuation of type  $D^+$  while other regions show both types ( $D^+$  and  $D^-$ ) depending on the out-of-plane fiber angle and other tissue properties like homogeneity or myelin sheath thickness.

**Keywords:** *dichroism; polarization; brain structures; nerve fiber architecture*

---

<sup>1</sup>Institute of Neuroscience and Medicine (INM-1), Forschungszentrum Jülich GmbH, 52425 Jülich, Germany. <sup>2</sup>Department of Physics, RWTH Aachen University, 52056 Aachen, Germany. <sup>3</sup>Cécile and Oskar Vogt Institute of Brain Research, University of Düsseldorf, 40204 Düsseldorf, Germany. <sup>4</sup>Zernike Institute for Advanced Materials, University of Groningen, 9747AG Groningen, the Netherlands. <sup>5</sup>Jülich Supercomputing Centre, Forschungszentrum Jülich GmbH, 52425 Jülich, Germany.

\* Correspondence and requests for material should be addressed to M.M. (email: [m.menzel@fz-juelich.de](mailto:m.menzel@fz-juelich.de))

**T**HE regular arrangements of nerve fibers and the highly ordered molecular structure of the surrounding myelin sheaths lead to optical anisotropy of brain tissue [1]. In previous work [2], we have studied the anisotropic attenuation of light (*diattenuation*) in unstained histological rat brain sections: the transmitted light intensity becomes maximal ( $I_{\max}$ ) for light polarized in a particular direction and minimal ( $I_{\min}$ ) for light polarized in the corresponding orthogonal direction. The *strength of the diattenuation* is defined as [3, 4]:  $|\mathcal{D}| \equiv (I_{\max} - I_{\min}) / (I_{\max} + I_{\min})$ . The direction of polarization (in the section plane) for which the transmitted light intensity becomes maximal is specified by the angle  $\varphi_D$ . By comparing  $\varphi_D$  to the in-plane orientation (*direction*) angle  $\varphi_P$  of the nerve fibers obtained from birefringence measurements (3D-PLI [5, 6]), we have found that there exist two different types of diattenuation that are regionally specific: in some brain regions, the transmitted light intensity becomes maximal when the light is polarized parallel to the nerve fibers ( $\varphi_D \approx \varphi_P$ , referred to as  $D^+$ ), in other brain regions, it becomes minimal ( $\varphi_D \approx \varphi_P + 90^\circ$ , referred to as  $D^-$ ). Why this effect occurs and how the type of diattenuation depends on the tissue composition were still open questions.

Here, we present diattenuation studies on brain tissue samples from different species that were obtained from brains cut along different anatomical planes to investigate how the observed diattenuation effects ( $D^+$  and  $D^-$ ) depend on the tissue structure. Furthermore, we explored the behavior of the diattenuation signal for aging tissue samples. To better understand the observed diattenuation effects and to learn more about how the diattenuation depends on the tissue properties, we simulated the diattenuation for different nerve fiber configurations using a finite-difference time-domain (FDTD) algorithm. Our simulations demonstrate that the diattenuation of brain tissue is caused by anisotropic absorption as well as by anisotropic scattering and that the type of diattenuation is related to the out-of-plane orientation (*inclination*) angle of the nerve fibers, but also on other tissue properties like the fiber orientation distribution or the myelin sheath thickness.

## RESULTS

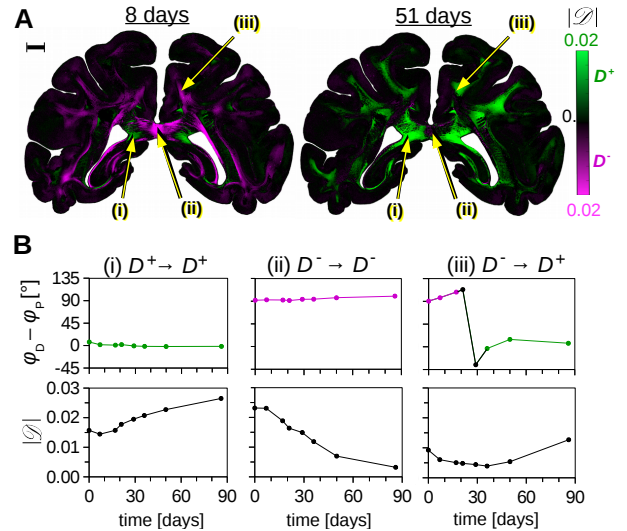
### Diattenuation for different species and fiber orientations.

Figure 2 shows the diattenuation images of coronal and sagittal brain sections with  $60\ \mu\text{m}$  thickness for a mouse and a rat brain (A) and a vervet monkey brain (B). The approximate orientation of the nerve fibers is known from brain atlases [7, 8] and 3D-PLI measurements [5, 6]. The diattenuation measurements were performed one day after tissue embedding (see *Methods*) with an effective object-space resolution of  $14\ \mu\text{m}/\text{px}$  (A) and  $27\ \mu\text{m}/\text{px}$  (B) using the *Large-Area Polarimeter (LAP)* [2]. A comparison between coronal and sagittal diattenuation images reveals that regions with diattenuation of type  $D^-$  (magenta) mostly belong to regions with in-plane fiber structures (coronal: cc, fi; sagittal: aci, cg, CPu), while regions with diattenuation of type  $D^+$  (green) mostly belong to regions with out-of-plane fiber structures (coronal: cg, df, sm, CPu; sagittal: cc, fi).

Measurements with a prototypic polarizing microscope with

$1.8\ \mu\text{m}/\text{px}$  yield similar  $D^+$  and  $D^-$  regions (see Supplementary Fig. 4), i.e. the observed diattenuation effects do not depend on the optical resolution of the imaging system.

**Diattenuation for aging tissue samples.** To study the diattenuation for aging tissue samples, a coronal section of a vervet monkey brain was measured 1, 8, 18, 22, 30, 37, 51, and 87 days after tissue embedding. Figure 1A shows the diattenuation maps 8 days and 51 days after tissue embedding. The size of the regions with diattenuation of type  $D^+$  (green) increases with increasing time after tissue embedding, while the size of the regions with diattenuation of type  $D^-$  (magenta) decreases. The yellow arrows mark a region that is already of type  $D^+$  directly after tissue embedding (i), a region that is still of type  $D^-$  after 51 days (ii), and a region that changes from type  $D^-$  to  $D^+$  with increasing time after embedding (iii). Figure 1B shows the corresponding values for  $(\varphi_D - \varphi_P)$  and  $|\mathcal{D}|$  for all eight measurements. In regions that show diattenuation of type  $D^+$  ( $D^-$ ), the strength of the diattenuation signal  $|\mathcal{D}|$  increases (decreases). The same behavior was also observed in brain sections from other species (e.g. human, see Supplementary Fig. 5).



**Fig. 1.** Diattenuation for aging brain tissue samples (coronal vervet monkey brain section with  $60\ \mu\text{m}$  thickness). (A) Diattenuation images measured 8 and 51 days after tissue embedding with an effective object-space resolution of  $43\ \mu\text{m}/\text{px}$  (Scale bar: 5 mm). Diattenuation values  $|\mathcal{D}|$  that belong to regions with diattenuation of type  $D^+$  ( $\varphi_D - \varphi_P \in [-20^\circ, 20^\circ]$ ) are shown in green, diattenuation values that belong to regions with diattenuation of type  $D^-$  ( $\varphi_D - \varphi_P \in [70^\circ, 110^\circ]$ ) are shown in magenta. The values  $\{|\mathcal{D}|, \varphi_D, \varphi_P\}$  were determined from polarimetric measurements with the LAP (see *Methods*). (B) Angle difference ( $\varphi_D - \varphi_P$ ) and strength of the diattenuation signal  $|\mathcal{D}|$  evaluated exemplary for three different regions (see yellow arrows): a region that is already of type  $D^+$  directly after tissue embedding (i), a region that is still of type  $D^-$  after 51 days (ii), and a region that changes from type  $D^-$  to  $D^+$  over time (iii). In regions with  $D^+$  ( $D^-$ ), the strength of the diattenuation increases (decreases) with increasing time after tissue embedding.

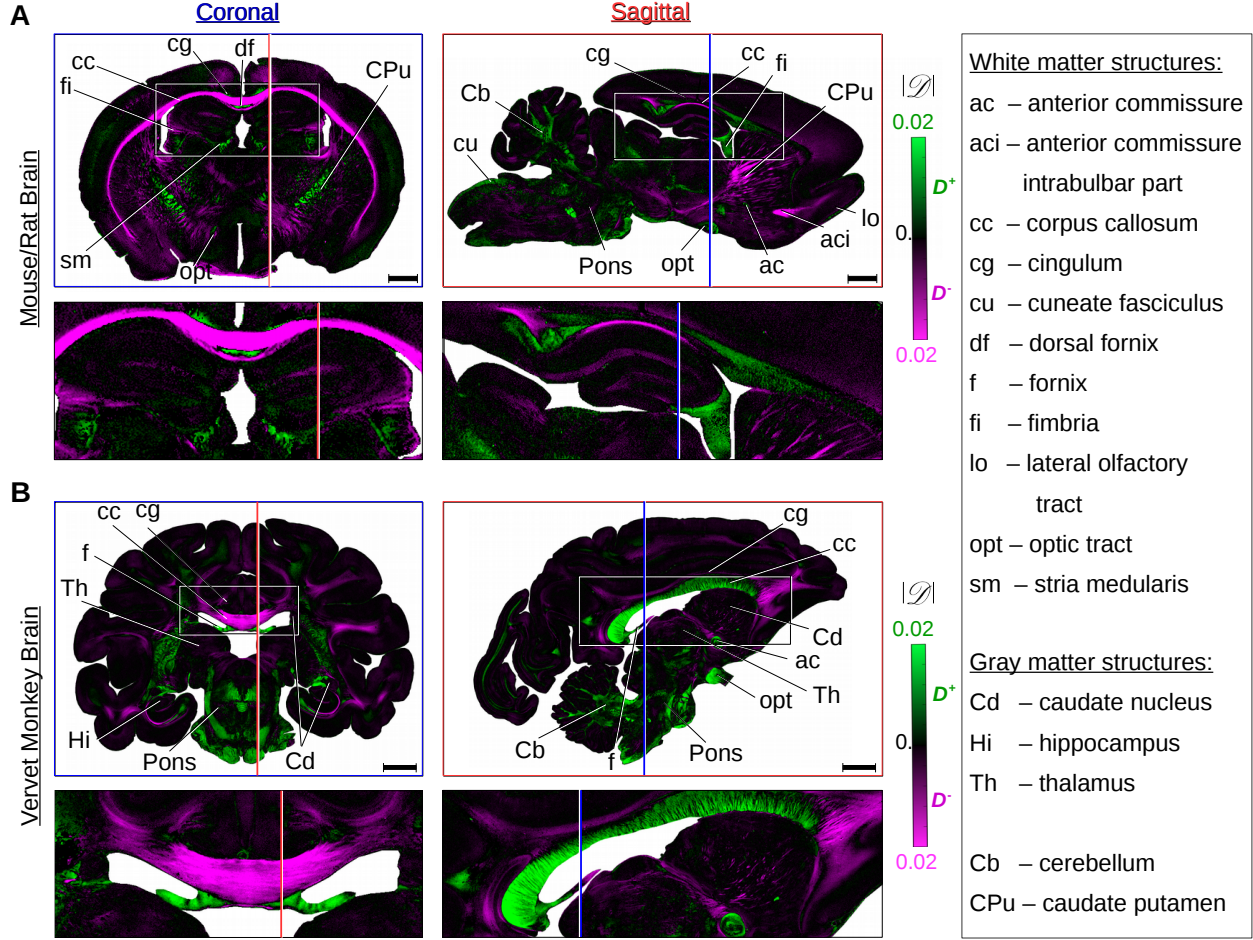


**Fig. 2.** Diattenuation images of coronal and sagittal brain sections with 60  $\mu\text{m}$  thickness. (A) Mouse brain (left) and rat brain (right) measured with an effective object-space resolution of 14  $\mu\text{m}/\text{px}$  (Scale bars: 1 mm). The diattenuation image of the rat brain section has already been shown in [2] (Fig. 9, s0175) in different colors. (B) Vervet monkey brain measured with an effective object-space resolution of 27  $\mu\text{m}/\text{px}$  (Scale bars: 5 mm). Selected anatomical structures are labeled according to rat [7] and vervet [8] brain atlases. The coronal (sagittal) section planes are indicated by blue (red) lines in the respective other brain section for reference. The strength of the diattenuation signal  $|\mathcal{D}|$  is shown in green for regions with diattenuation of type  $D^+$  ( $\varphi_D - \varphi_P \in [-20^\circ, 20^\circ]$ ) and in magenta for regions with diattenuation of type  $D^-$  ( $\varphi_D - \varphi_P \in [70^\circ, 110^\circ]$ ). The values  $\{|\mathcal{D}|, \varphi_D, \varphi_P\}$  were obtained from polarimetric measurements with the LAP (see [Methods](#)) one day after tissue embedding. Regions with  $D^-$  mostly belong to regions with flat fiber structures (with respect to the section plane), while regions with  $D^+$  mostly belong to regions with steep fiber structures.

### Simulated diattenuation for different fiber configurations.

We performed FDTD simulations (see [Methods](#)) to model and better understand the observed diattenuation effects. Diattenuation caused by anisotropic absorption (dichroism  $D_K$ ) was described by an analytical model (see [Supplementary Note 1](#)). The diattenuation caused by anisotropic scattering ( $D_S$ ) was computed from the simulated transmitted intensity of light polarized along the x- and y-axes:  $D_S = (I_x - I_y)/(I_x + I_y)$ , where the symmetry axis of the sample (projected onto the xy-plane) is aligned with the x-axis of the system. The magnitude of  $D_S$  is related to the strength of the diattenuation ( $|D_S| \approx |\mathcal{D}|$ ), the sign indicates the phase  $\varphi_D$ : positive (negative) values correspond to regions with  $D^+$  ( $D^-$ ) in which the transmitted light intensity becomes maximal when the light is polarized parallel (perpendicularly) to the fiber structure, i. e. in the x-(y-)direction.

To better understand how the diattenuation depends on the fiber inclination, we simulated the diattenuation im-

ages for fiber bundles with different inclination angles ( $\alpha = \{0^\circ, 10^\circ, \dots, 90^\circ\}$ ): a bundle with broad fiber orientation distribution and a bundle of densely grown fibers (see [Fig. 3A](#)). [Figure 3B](#) shows the diattenuation images for the bundle of densely grown fibers for  $\alpha = 0^\circ$  and  $80^\circ$ . The diattenuation images for all inclination angles are shown in [Supplementary Fig. 6](#). The diattenuation is mostly negative (magenta) for flat fibers ( $\alpha \leq 50^\circ$ ) and becomes more positive (green) for steep fibers ( $\alpha > 60^\circ$ ).

[Figure 3C](#) shows the simulated diattenuation curves (mean value of  $D_S$  plotted against  $\alpha$ ) for both fiber bundles: The mean diattenuation  $\bar{D}_S$  is negative for non-steep fibers ( $\alpha \leq 60^\circ$ ), positive for steep fibers ( $70^\circ < \alpha < 90^\circ$ ), and almost zero for vertical fibers. For the bundle with broad fiber orientation distribution (red curve), the values range from  $\bar{D}_S \approx -12.4\%$  to  $1.2\%$ . For the bundle of densely grown fibers (orange curve), the range is much larger ( $\bar{D}_S \approx -22\%$  to  $10\%$ ).

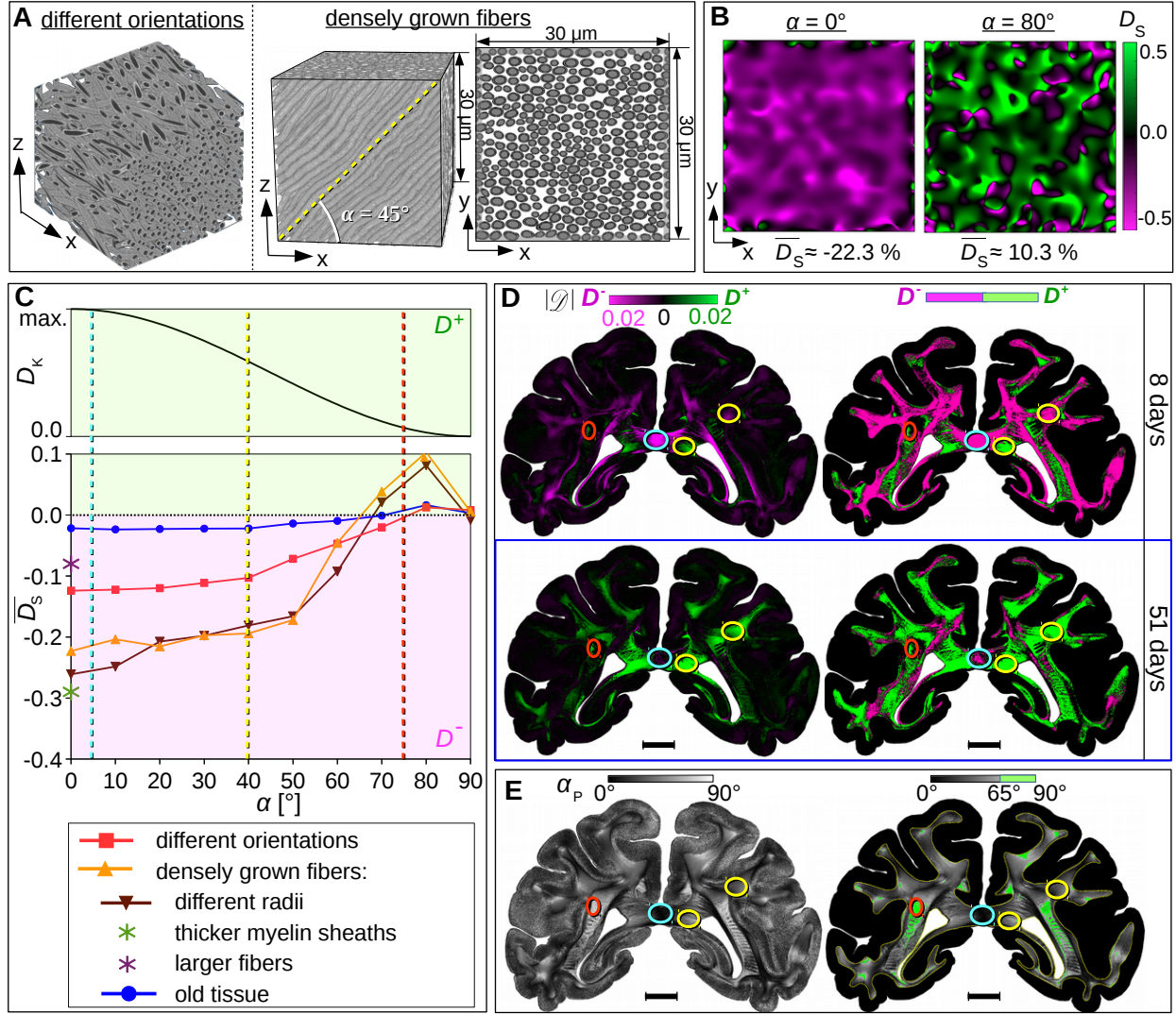


**Fig. 3.** Comparison of simulated and measured diattenuation effects. (A) Fiber bundles used for FDTD simulations (shown exemplary for an inclination angle  $\alpha$ ): a bundle with broad fiber orientation distribution ( $\alpha = 0^\circ$ ) and a bundle of densely grown fibers ( $\alpha = 45^\circ$ ). (B) Simulated diattenuation images  $D_S$  and mean values  $\bar{D}_S$  for the bundle of densely grown fibers shown exemplary for  $\alpha = 0^\circ$  and  $80^\circ$  (the complete set of diattenuation images can be found in Supplementary Fig. 6B). (C) Diattenuation caused by anisotropic absorption (dichroism  $D_K$ ) and by anisotropic scattering ( $D_S$ ) plotted against the inclination angle  $\alpha$ . The curve for  $D_K$  was computed analytically using  $D_K = \tanh(0.05 \cos^2 \alpha)$  (see Supplementary Note 1 for derivation). The curves for  $\bar{D}_S$  were computed from FDTD simulations (see Methods) for the bundle with broad fiber orientation distribution (red curve) and the bundle of densely grown fibers (orange curve) for fibers with radii  $r \in [0.5, 0.8] \mu\text{m}$ , myelin sheath thickness  $t_{\text{sheath}} = 0.35 r$ , and myelin refractive index  $n_m = 1.47$ . The bundle of densely grown fibers was also simulated for a broader distribution of radii ( $r \in [0.3, 1.0] \mu\text{m}$ , brown curve), for thicker myelin sheaths ( $t_{\text{sheath}} = 0.6 r$ , green star), for larger fibers ( $r \in [2.5, 4.0] \mu\text{m}$ , magenta star), and for a reduced myelin refractive index which models old tissue samples ( $n_m = 1.39$ , blue curve). Positive diattenuation values (corresponding to type  $D^+$ ) are shown on a green background, diattenuation values (corresponding to type  $D^-$ ) are shown on a magenta background. Supplementary Fig. 7 shows the simulated diattenuation values  $\bar{D}_S$  plotted against the fiber properties (fiber radius distribution, myelin sheath thickness, fiber size, myelin refractive index) for the horizontal bundle of densely grown fibers. (D) Diattenuation images of a coronal vervet brain section measured 8 and 51 days after tissue embedding (adapted from Fig. 1A). Diattenuation values  $|\mathcal{D}|$  that belong to regions with diattenuation of type  $D^+$  ( $\varphi_D - \varphi_P \in [-20^\circ, 20^\circ]$ ) are shown in green, diattenuation values that belong to regions with diattenuation of type  $D^-$  ( $\varphi_D - \varphi_P \in [70^\circ, 110^\circ]$ ) are shown in magenta, regions that cannot clearly be assigned are shown in black. The images on the left were weighted with the strength of the diattenuation signal  $|\mathcal{D}|$ , the images on the right show the  $D^+$  and  $D^-$  regions in the white matter without any weighting. (E) Corresponding inclination angles  $\alpha_P$  obtained from a 3D-PLI measurement with tilting (see Methods). The image on the right only shows the inclination angles in the white matter and regions with  $\alpha_P > 65^\circ$  are marked in green. The dashed vertical lines in C and the colored circles in D and E highlight regions with flat, intermediate, and steep fiber inclinations:  $\alpha = 5^\circ$  (cyan),  $\alpha = 40^\circ$  (yellow), and  $\alpha = 75^\circ$  (red). As predicted by the simulations, regions with steep fibers only show diattenuation of type  $D^+$  while regions with flat fibers are more likely to show diattenuation of type  $D^-$ . With increasing time after tissue embedding (i. e. with lower myelin refractive index), the fraction of regions with diattenuation of type  $D^-$  becomes less. (Scale bars: 5 mm)

The fibers were modeled with radii  $r \in [0.5, 0.8] \mu\text{m}$ , consisting of an inner axon and a surrounding myelin sheath with thickness  $t_{\text{sheath}} = 0.35r$  (see *Methods*). To study how the diattenuation depends on the fiber properties, the bundle of densely grown fibers was also simulated for a broader distribution of fiber radii ( $r \in [0.3, 1.0] \mu\text{m}$ , brown curve), thicker myelin sheaths ( $t_{\text{sheath}} = 0.6r$ , green star), and larger fibers ( $r \in [2.5, 4.0] \mu\text{m}$ , magenta star). While different fiber radii yield similar diattenuation curves (see also Supplementary Fig. 7A), thicker myelin sheaths lead to more negative and larger fibers to less negative diattenuation values for  $\alpha = 0^\circ$  (see also Supplementary Fig. 7B and C).

To estimate the combined diattenuation effect of  $D_S$  and  $D_K$ , Fig. 3C shows the simulated diattenuation curves  $\overline{D_S}$  in direct comparison to the dichroism  $D_K > 0$  (see Supplementary *Note1* for derivation) plotted against the fiber inclination angle  $\alpha$ : For regions with non-steep fibers ( $\alpha < 65^\circ$ ), both diattenuation of type  $D^+$  and  $D^-$  are observed, depending on whether  $D_K > 0$  or  $D_S < 0$  dominates. Regions with steep fibers ( $65^\circ < \alpha < 90^\circ$ ) only show diattenuation of type  $D^+$  because both  $D_S$  and  $D_K$  are positive. As expected, regions with vertical fibers ( $\alpha = 90^\circ$ ) show small diattenuation values ( $|D_S|, |D_K| \ll 1$ ).

**Simulated diattenuation for aging tissue samples.** With increasing time after embedding the brain sections, the surrounding glycerin solution presumably soaks into the myelin sheaths and reduces their effective refractive index. So far, the simulations were performed for a myelin refractive index of 1.47, corresponding to literature values (see *Methods*). To model the diattenuation of brain tissue with long embedding time, the bundle of densely grown fibers was simulated for a reduced myelin refractive index of 1.39 (see Fig. 3C, blue curve): the strength of the simulated diattenuation signals is much less ( $\overline{D_S} \approx -2.2\%$  to  $1.6\%$ ). Supplementary Fig. 7D shows that  $|D_S|$  decreases with decreasing myelin refractive index. This suggests that anisotropic scattering decreases with increasing time after tissue embedding. As dichroism  $D_K$  is expected to remain positive, the net observed diattenuation is expected to become more positive over time.

## DISCUSSION

In previous work, we have shown that brain tissue exhibits two different types of diattenuation: in some regions, the light is minimally attenuated when it is polarized parallel to the nerve fibers ( $D^+$ ), in others, it is maximally attenuated ( $D^-$ ). Here, we investigated this effect both in experimental and simulation studies and demonstrated that it depends on nerve fiber orientation, tissue composition, and embedding time.

Our experimental studies show that the same diattenuation effects can be observed in different species (mouse, rat, monkey, human) and at different optical resolutions (from  $43 \mu\text{m}/\text{px}$  to  $1.8 \mu\text{m}/\text{px}$ ): regions with out-of-plane fibers show almost exclusively diattenuation of type  $D^+$ , while regions with in-plane fibers are more likely to show diattenuation of type  $D^-$  (see Fig. 2) which decreases with increasing time after tissue embedding (see Fig. 1).

Using a combination of analytical modeling and FDTD simulations, we could explain the experimental observations. The

diattenuation caused by anisotropic absorption (dichroism) was described by an analytical model (see Eq. (19) in Supplementary *Note1*): according to this model, the dichroism decreases with increasing out-of-plane inclination angle of the nerve fibers, only causes positive diattenuation (type  $D^+$ ), and does not depend on tissue aging. The diattenuation caused by anisotropic scattering was simulated for various fiber bundles with different inclination angles: regions with flat fibers show diattenuation of type  $D^-$  while regions with steep fibers show diattenuation of type  $D^+$ . The strength of the simulated diattenuation signal depends on tissue properties like fiber orientation distribution and myelin sheath thickness, and decreases in aging tissue samples (see Fig. 3C). To directly compare our simulation results to the experimental observations, we evaluated the diattenuation maps of the coronal vervet brain section in Fig. 1A in regions with different fiber inclinations (see Fig. 3D and E). In order to better compare the  $D^+$  and  $D^-$  regions to the fiber inclination, the brain sections on the right only show the white matter regions without any weighting. Regions with diattenuation of type  $D^+$  and regions with fiber inclinations  $> 65^\circ$  are shown in green, while regions with diattenuation of type  $D^-$  are shown in magenta. In freshly embedded brain sections, regions with steep fibers ( $\alpha_p > 65^\circ$ ) show almost exclusively type  $D^+$ : nearly all green regions in Fig. 3E are also green in Fig. 3D (see red circles). Regions with lower fiber inclinations show both types  $D^+$  and  $D^-$  (see yellow circles). Regions with flat fiber inclinations are most likely to show type  $D^-$  (see cyan circles). All these observations can be explained by the combined model of analytically computed and simulated diattenuation curves (the dashed vertical lines in Fig. 3C mark the inclination angles of the evaluated regions).

The diattenuation for aging tissue samples could successfully be modeled by assuming that the embedding glycerin solution soaks into the myelin sheaths of the nerve fibers and reduces the effective refractive index of myelin: the simulations have shown that a reduced myelin refractive index leads to a reduced anisotropic scattering (cf. orange and blue curves in Fig. 3C), i. e. brain tissue with long embedding time shows a smaller fraction of regions with diattenuation of type  $D^-$  (cf. Fig. 3D). The same model was used in [9] to explain the increasing transparency of aging brain tissue samples.

The finding that  $D_K$  is positive means that the absorption becomes maximal when the light is polarized perpendicularly to the nerve fiber axis, i. e. in the plane of the lipid molecules in the myelin sheath (cf. Supplementary *Note1*). This suggests that the dichroism of brain tissue is mainly caused by the myelin lipids.

Our simulations show that the strength and type of diattenuation ( $D^+/D^-$ ) depend not only on the out-of-plane inclination angle of the nerve fibers in the investigated brain sections and on the time after tissue embedding, but also on other tissue properties like the fiber orientation distribution or the myelin sheath thickness (cf. Fig. 3C). How the measured type of diattenuation can be related to underlying tissue properties should be investigated in future studies.

In conclusion, we could show that the diattenuation of brain tissue provides image contrasts between different tissue types and can therefore be used in addition to other image modalities to learn more about the brain's nerve fiber and tissue composition.

## METHODS

**Preparation of Brain Sections.** The measurements were performed on healthy brains from different species: mouse (*C57BL/6*, male, six months old), rat (*Wistar*, male, three months old), vervet monkey (African green monkey: *Chlorocebus aethiops sabaeus*, male, between one and two years old), and human (male, 87 years old). All animal procedures were approved by the institutional animal welfare committee at Forschungszentrum Jülich GmbH, Germany, and were in accordance with European Union (National Institutes of Health) guidelines for the use and care of laboratory animals.

The brains were removed from the skull within 24 hours after death, fixed with 4% buffered formaldehyde for several weeks, immersed in solutions of 10% and 20% glycerin combined with 2% Dimethyl sulfoxide for cryo-protection, and deeply frozen. The frozen brains were cut with a cryostat microtome (*Leica Microsystems*, Germany) into sections of 60  $\mu\text{m}$ . The brain sections were mounted on glass slides, embedded in a solution of 20% glycerin, and cover-slipped. The brain sections were measured one day after embedding (freshly embedded sections) or after several days to study the diattenuation signal in aging tissue samples.

**Polarimetric Measurements.** The measurements were performed with the in-house developed *Large-Area Polarimeter (LAP)* which was also used for the diattenuation studies by MENZEL, RECKFORT *et al.* [2]. The LAP consists of a green light source ( $\lambda = (525 \pm 25) \text{ nm}$ ), a pair of crossed linear polarizers, and a quarter-wave retarder and specimen stage mounted in between the polarizers. During a measurement, the polarizers and the retarder were rotated simultaneously by angles  $\rho = \{0^\circ, 10^\circ, \dots, 170^\circ\}$  and the transmitted light intensity  $I(\rho)$  was recorded by a CCD camera with the microscanning procedure of the camera sensor, yielding  $4164 \times 3120$  pixels with a resolution down to 14  $\mu\text{m}/\text{px}$ .

The in-plane orientation angles  $\varphi_P$  of the nerve fibers were obtained from 3D-PLI measurements [5, 6] with the above setup and by performing a discrete harmonic Fourier analysis on the measured light intensities per image pixel ( $I_P(\rho) = a_{0P} + a_{2P} \cos(2\rho) + b_{2P} \sin(2\rho)$ ) and evaluating the phase of the signal:  $\varphi_P = \text{atan2}(-a_{2P}, b_{2P})/2$ . The amplitude of the signal is related to the phase shift  $\delta_P$  induced by the birefringent brain section ( $|\sin \delta_P| = (a_{2P}^2 + b_{2P}^2)^{1/2}/a_{0P}$ ,  $\delta_P \propto \cos^2 \alpha_P$  [1]) and was used to compute the out-of-plane inclination angles  $\alpha_P$  of the fibers in Fig. 3E, making use of the tiltable specimen stage [10] to improve the determination of the inclination angles.

The diattenuation measurements [2] were performed by removing the retarder and the second polarizer from the light path and measuring the transmitted light intensities as described above. To account for the lower signal-to-noise ratio, the image of the brain section was recorded 20 times for each filter position and averaged. The strength of the measured diattenuation signal  $|\mathcal{D}|$  and the phase  $\varphi_D$  were determined from the amplitude and phase of the resulting light intensity profile ( $I_D(\rho) = a_{0D} + a_{2D} \cos(2\rho) + b_{2D} \sin(2\rho)$ ):  $|\mathcal{D}| = (a_{2D}^2 + b_{2D}^2)^{1/2}/a_{0D}$  and  $\varphi_D = \text{atan2}(b_{2D}, a_{2D})/2$ .

The Fourier coefficients of order zero  $\{a_{0P}, a_{0D}\}$  were used to register the images of the 3D-PLI measurements onto the images of the diattenuation measurements using in-house developed software tools which perform linear and non-linear transformations.

The resulting images  $\{\varphi_P, |\mathcal{D}|, \varphi_D\}$  were used to generate the diattenuation images:  $|\mathcal{D}|$  values belonging to regions with  $(\varphi_D - \varphi_P) \in [-20^\circ, 20^\circ]$  were colored in green (referred to as  $D^+$ ), regions with  $(\varphi_D - \varphi_P) \in [-70^\circ, 110^\circ]$  were colored in magenta (referred to as  $D^-$ ). The angle ranges account for the uncertainties of  $\varphi_D$  due to the non-ideal optical properties of the LAP [2].

**Measurements with Prototypic Polarizing Microscope.** The prototypic polarizing microscope has been described by WIESE *et al.* [11]. It consists of a green light source ( $\lambda = (532 \pm 5) \text{ nm}$ ), a rotatable polarizer, a fixed circular analyzer (quarter-wave retarder with linear polarizer), and a CCD camera. The polarizing filters are of higher quality

than in the LAP. The microscope objective has a  $4\times$  magnification and a numerical aperture of 0.2, yielding a pixel size in object space of about 1.8  $\mu\text{m}$ . The polarimetric measurements were performed as described above. Due to a superior signal-to-noise ratio, repeated diattenuation measurements were not necessary.

**Model of Nerve Fiber Configurations.** The fiber bundles used for the FDTD simulations (cf. Fig. 3A) were generated by in-house developed software similar to [12], allowing to create densely packed fibers without intersections: 700 straight fibers with different radii were randomly uniformly placed in an area of  $45 \times 30 \mu\text{m}^2$  and divided into segments of 2–5  $\mu\text{m}$ . The fiber segments were assigned a random displacement in  $x, y, z$  (max. 10  $\mu\text{m}$  for the bundle with broad fiber orientation distribution, max. 1  $\mu\text{m}$  for the bundle of densely grown fibers). The resulting fiber segments were split or merged until the length of each segment was again between 2–5  $\mu\text{m}$ , ensuring that the maximum angle between adjacent segments was less than  $20^\circ$ . When a collision between two segments was detected, the segments were exposed to a small repelling force and the previous step was repeated until no more collisions were detected. The mode angle difference between the local fiber orientation vectors and the predominant orientation of the resulting fiber bundle is about  $25^\circ$  for the bundle with broad fiber orientation distribution and less than  $10^\circ$  for the bundle of densely grown fibers. To generate fiber bundles with different inclination angles, the bundles were rotated around the  $y$ -axis with respect to the center position and cropped to a volume of  $30 \times 30 \times 30 \mu\text{m}^3$ . To prevent fibers from touching each other after discretization, all diameters were reduced by 5%.

The simulations were performed with the same simplified nerve fiber model used in [9] to simulate 3D-PLI measurements: Each fiber with radius  $r$  was modeled by an inner axon ( $r_{\text{ax}} = 0.65r$ ) and a surrounding myelin sheath with thickness  $t_{\text{sheath}} = 0.35r$  consisting of two myelin (lipid) layers ( $t_m = 3/7 t_{\text{sheath}}$ ) and a separating glycerin layer ( $t_g = 1/7 t_{\text{sheath}}$ ). The myelin sheath thickness contributes approximately one third to the overall fiber radius [13]. The refractive indices of axon, myelin and glycerin layers were estimated from literature values of cytoplasm ( $n_{\text{ax}} = 1.35$  [14]), lipids/membranes ( $n_m = 1.47$  [15]), and from refractive index measurements of the glycerin solution used for embedding the brain sections ( $n_g = 1.37$ , measured with digital refractometer). The surrounding medium was assumed to be homogeneous with a refractive index  $n_{\text{surr}} = 1.37$ , corresponding to the refractive index of gray matter [16]. The absorption coefficients of brain tissue are small [17, 18] and were therefore neglected.

The fibers shown in Fig. 3A have radii between 0.5  $\mu\text{m}$  and 0.8  $\mu\text{m}$  and a myelin sheath thickness of 0.35  $r$ . The bundle of densely grown fibers was also simulated for different values of  $r$ ,  $t_{\text{sheath}}$ , and  $n_m$  (see Figs. 3C and 7).

**FDTD Simulations.** The propagation of the polarized light wave through the sample was computed by *TDME3D*<sup>TM</sup> [19, 20] – a massively parallel three-dimensional Maxwell Solver based on a conditionally stable finite-difference time-domain (FDTD) algorithm [21, 22]. The algorithm numerically computes the electromagnetic field components by discretizing space and time and approximating Maxwell's curl equations by finite differences [23].

The sample contains the fiber configuration ( $30 \times 30 \times 30 \mu\text{m}^3$ , see above) and 0.5  $\mu\text{m}$  thick layers of glycerin solution on top and at the bottom. The dimensions of the simulation volume are  $30 \times 30 \times 35 \mu\text{m}^3$ , including 1  $\mu\text{m}$  thick uniaxial perfectly matched layer absorbing boundaries. The different components of the sample were modeled as dielectrics with real refractive indices (defined above). The sample was illuminated by a plane monochromatic wave with linear polarization (along the  $x$ - or  $y$ -axis). The simulations were performed on the supercomputer *JUQUEEN* [24] at Forschungszentrum Jülich GmbH, Germany, with 200 time steps, a Courant factor of 0.8, and a Yee mesh size of 25 nm. Using an MPI grid of  $16 \times 16 \times 16$ , each simulation run (calculation of one configuration and one polarization state) consumed between 7000–8000 CPU hours, required a minimum memory between 260–360 GB, and lasted between 1:45–2:00 hours.

The polarimeter used for the measurements (LAP) has a broad wavelength spectrum and emits mostly incoherent light under different angles of incidence. As each simulation run is performed with coherent light with a certain wavelength and angle of incidence, the LAP is not well suited to be modeled by FDTD simulations. Instead, we performed the simulations for the imaging system of the *Polarizing Microscope (PM)* [5, 6], like the simulations of the 3D-PLI measurement in [9]. The PM (manufactured by *Taorad GmbH*, Germany) contains higher quality components and uses more coherent and less diffusive light with  $\lambda = (550 \pm 5)$  nm. As the polarizing filters cannot be removed, the PM cannot be used for diattenuation measurements. However, the optics of the PM are similar to those of the prototypic polarizing microscope (the microscope objective has a  $5\times$  magnification, a numerical aperture of 0.15, and yields an object-space resolution of  $1.33 \mu\text{m}/\text{px}$ ). Therefore, the diattenuation effects simulated for the optics of the PM are presumably similar to those observed in the measurements.

The imaging system of the PM was simulated as described in [9]: The simulations were performed for normally incident light with 550 nm wavelength. The numerical aperture (NA) was modeled by considering only wave vector angles  $\leq \arcsin(\text{NA}) \approx 8.6^\circ$ . The spherical microlenses of the camera sensor were modeled by applying a moving average over the area of the microlens with a diameter of  $1.33 \mu\text{m}$ . The light intensity recorded by the camera was computed as the absolute squared value of the electric field vector (neglecting angle dependencies because of the small aperture). To obtain the intensity at a certain point in the image plane, the electric field vectors for different wave vectors were summed and averaged over time.

To model the diattenuation measurement, the simulations were performed for light polarized along the x-axis and along the y-axis. The resulting light intensities ( $I_x$  and  $I_y$ ) were used to compute the diattenuation images:  $D_S = (I_x - I_y)/(I_x + I_y)$ .

## REFERENCES

- [1] M. Menzel, K. Michielsen, H. De Raedt, J. Reckfort, K. Amunts, and M. Axer. A Jones matrix formalism for simulating three-dimensional polarized light imaging of brain tissue. *Journal of the Royal Society Interface*, 12:20150734, 2015. doi: 10.1098/rsif.2015.0734.
- [2] M. Menzel, J. Reckfort, D. Weigand, H. Köse, K. Amunts, and M. Axer. Diattenuation of brain tissue and its impact on 3D polarized light imaging. *Biomedical Optics Express*, 8(7):3163–3197, 2017. doi: 10.1364/BOE.8.003163.
- [3] R. A. Chipman. Polarimetry. In *Handbook of Optics, Vol. 2: Devices, Measurements, and Properties*, chapter 22, pages 22.1–22.37. McGraw-Hill, New York, 2 edition, 1994. ISBN 978-0070479746.
- [4] D. B. Chenault and R. A. Chipman. Measurements of linear diattenuation and linear retardance spectra with a rotating sample spectropolarimeter. *Applied Optics*, 32(19):3513–3519, 1993. doi: 10.1364/AO.32.003513.
- [5] M. Axer, K. Amunts, D. Grässel, C. Palm, J. Dammers, H. Axer, U. Pietrzyk, and K. Zilles. A novel approach to the human connectome: Ultra-high resolution mapping of fiber tracts in the brain. *NeuroImage*, 54(2):1091–1101, 2011. doi: 10.1016/j.neuroimage.2010.08.075.
- [6] M. Axer, D. Grässel, M. Kleiner, J. Dammers, T. Dickscheid, J. Reckfort, T. Hütz, B. Eiben, U. Pietrzyk, K. Zilles, and K. Amunts. High-resolution fiber tract reconstruction in the human brain by means of three-dimensional polarized light imaging. *Frontiers in Neuroinformatics*, 5(34):1–13, 2011. doi: 10.3389/fninf.2011.00034.
- [7] G. Paxinos and C. Watson. *The Rat Brain in Stereotaxic Coordinates*. Academic Press, 6 edition, 2007.
- [8] R. P. Woods, S. C. Fears, M. J. Jorgensen, L. A. Fairbanks, A. W. Toga, and N. B. Freimer. A web-based brain atlas of the vervet monkey, *chlorocebus aethiops*. *NeuroImage*, 54(3):1872–1880, 2011. doi: 10.1016/j.neuroimage.2010.09.070.
- [9] M. Menzel, M. Axer, H. De Raedt, I. Costantini, L. Silvestri, F. S. Pavone, K. Amunts, and K. Michielsen. Transmittance assisted interpretation of nerve fiber orientations. *arXiv:1806.07157v1*, 2018.
- [10] H. Wiese, D. Grässel, U. Pietrzyk, K. Amunts, and M. Axer. Polarized light imaging of the human brain: a new approach to the data analysis of tilted sections. In D. B. Chenault and D. H. Goldstein, editors, *SPIE Proceedings, Polarization: Measurement, Analysis, and Remote Sensing XI*, volume 9099, 2014. doi: 10.1117/12.2053305.
- [11] H. Wiese. *Enhancing the Signal Interpretation and Microscopical Hardware Concept of 3D Polarized Light Imaging*. PhD thesis, University of Wuppertal, 2016.
- [12] L. Chapelle, M. Lévesque, P. Brøndsted, M. R. Foldschack, and Y. Kusano. Generation of non-overlapping fiber architecture. In *Proceedings of the 20th International Conference on Composite Materials ICCM20 Secretariat*, 2015.
- [13] P. Morell, R. H. Quarles, and W. T. Norton. Formation, structure, and biochemistry of myelin. In G. J. Siegel, editor, *Basic Neurochemistry - Molecular, Cellular, and Medical Aspects*, pages 109–136. Raven Press, New York, 4 edition, 1989. ISBN 0881673439.
- [14] F. A. Duck. *Physical Properties of Tissue: A Comprehensive Reference Book*. Academic Press, San Diego, 1990. ISBN 9780122228001.
- [15] H.-J. van Manen, P. Verkuijlen, P. Wittendorp, V. Subramaniam, T. K. van den Berg, D. Roos, and C. Otto. Refractive index sensing of green fluorescent proteins in living cells using fluorescence lifetime imaging microscopy. *Biophysical Letters*, 94(8):L67–69, 2008. doi: 10.1529/biophysj.107.127837.
- [16] Jingjing Sun, Sung Jin Lee, Lei Wu, Malisa Sarntinoranont, and Huikai Xie. Refractive index measurement of acute rat brain tissue slices using optical coherence tomography. *Optics Express*, 20(2):1084–1095, 2012. doi: 10.1364/OE.20.001084.
- [17] H.-J. Schwarzmaier, A. Yaroslavsky, I. Yaroslavsky, T. Goldbach, T. Kahn, F. Ulrich, P. C. Schulze, and R. Schober. Optical properties of native and coagulated human brain structures. *SPIE*, 2970: 492–499, 1997. doi: 10.1117/12.275082.
- [18] A. N. Yaroslavsky, P. C. Schulze, I. V. Yaroslavsky, R. Schober, F. Ulrich, and H.-J. Schwarzmaier. Optical properties of selected native and coagulated human brain tissues in vitro in the visible and near infrared spectral range. *Physics in Medicine and Biology*, 47:2059–2073, 2002. URL <http://stacks.iop.org/PMB/47/2059>.
- [19] K. Michielsen, H. de Raedt, and D. G. Stavenga. Reflectivity of the gyroid biophotonic crystals in the ventral wing scales of the Green Hairstreak butterfly, *Callophrys rubi*. *Journal of the Royal Society Interface*, 7:765–771, 2010. doi: 10.1098/rsif.2009.0352.
- [20] B. D. Wilts, K. Michielsen, H. De Raedt, and D. G. Stavenga. Sparkling feather reflections of a bird-of-paradise explained by finite-difference time-domain modeling. *Proceedings of the National Academy of Sciences*, 2014. doi: 10.1073/pnas.1323611111.
- [21] A. Taflove and S. C. Hagness. *Computational Electrodynamics: The Finite-Difference Time-Domain Method*. Artech House, MA USA, 3 edition, 2005. ISBN 1580538320.

- [22] H. De Raedt. Advances in unconditionally stable techniques. In A. Taflove and S. C. Hagness, editors, *Computational Electrodynamics: The Finite-Difference Time-Domain Method*, chapter 18. Artech House, MA USA, 3 edition, 2005. ISBN 1580538320.
- [23] M. Menzel, M. Axer, H. De Raedt, and K. Michielsen. Finite-Difference Time-Domain Simulation for Three-Dimensional Polarized Light Imaging. In K. Amunts, L. Grandinetti, T. Lippert, and N. Petkov, editors, *Brain-Inspired Computing. Brain-Comp 2015. Lecture Notes in Computer Science*, volume 10087, chapter 6, pages 73–85. Springer International Publishing, Cham, 2016. doi: [10.1007/978-3-319-50862-7\\_6](https://doi.org/10.1007/978-3-319-50862-7_6).
- [24] Jülich Supercomputing Centre. JUQUEEN: IBM Blue Gene/Q Supercomputer System at the Jülich Supercomputing Centre. *Journal of large-scale research facilities*, 1,A1, 2015. doi: [10.17815/jlsrf-1-18](https://doi.org/10.17815/jlsrf-1-18).
- [25] Jülich Supercomputing Centre. JURECA: General-purpose supercomputer at Jülich Supercomputing Centre. *Journal of large-scale research facilities*, 2(A62), 2016. doi: [10.17815/jlsrf-2-121](https://doi.org/10.17815/jlsrf-2-121).
- [26] M. Born and E. Wolf. *Principles of Optics - Electromagnetic Theory of Propagation, Interference and Diffraction of Light*. Cambridge University Press, 7 edition, 2011. ISBN 978-0-521-64222-4.
- [27] N. Ghosh and I. A. Vitkin. Tissue polarimetry: concepts, challenges, applications, and outlook. *Journal of Biomedical Optics*, 16(11):110801, 2011. doi: [10.1117/1.3652896](https://doi.org/10.1117/1.3652896).
- [28] J. Beuthan, O. Minet, J. Helfmann, M. Herrig, and G. Müller. The spatial variation of the refractive index in biological cells. *Physics in Medicine and Biology*, 41(3):369–382, 1996.
- [29] W. Demtröder. *Experimentalphysik 2 - Elektrizität und Optik*. Springer-Verlag Berlin Heidelberg, 5 edition, 2009. ISBN 978-3-540-68210-3.

## ACKNOWLEDGMENTS

This project has received funding from the Helmholtz Association portfolio theme ‘*Supercomputing and Modeling for the Human Brain*’, from the European Union’s Horizon 2020 Research and Innovation Programme under Grant Agreement No. 720270 (HBP SGA1), and from the National Institutes of Health under grant agreements No. R01MH092311 and 5P40OD010965. We gratefully acknowledge the computing time granted by the JARA-HPC Vergabegremium and VSR commission on the supercomputer *JURECA* [25] and the JARA-HPC Partition part of the supercomputer *JUQUEEN* [24] at Forschungszentrum Jülich GmbH. We thank Markus Cremer, Christian Schramm, and Patrick Nysten for the preparation of the histological brain sections, Julia Reckfort, Hasan Köse, David Gräbel, Isabelle Mafoppa Fomat, and Philipp Schlömer for the polarimetric measurements, Felix Matuschke for providing the algorithm to generate the fiber configurations, and Taorad GmbH, Germany, for providing the optical bench and equipment for the high-resolution diattenuation measurements.

## AUTHOR CONTRIBUTIONS

M.M. substantially contributed to the conception and design of the study as well as to the analysis and interpretation of the experimental and simulated data and to the theoretical considerations. She analyzed the measurements, carried out the simulations, created the figures, and wrote the manuscript. M.A. participated in the conception and design of the study, contributed to the analysis and interpretation of the data, and to the revision of the manuscript. K.A. contributed to the anatomical content of the study. H.D.R. contributed to the interpretation of the simulated data, to the theoretical considerations, and to the revision of the manuscript. K.M. participated in the design of the study, contributed to the interpretation of the simulated data, to the theoretical considerations, and to the revision of the manuscript. All authors read the final manuscript and gave approval for publication.

SUPPLEMENTARY INFORMATION

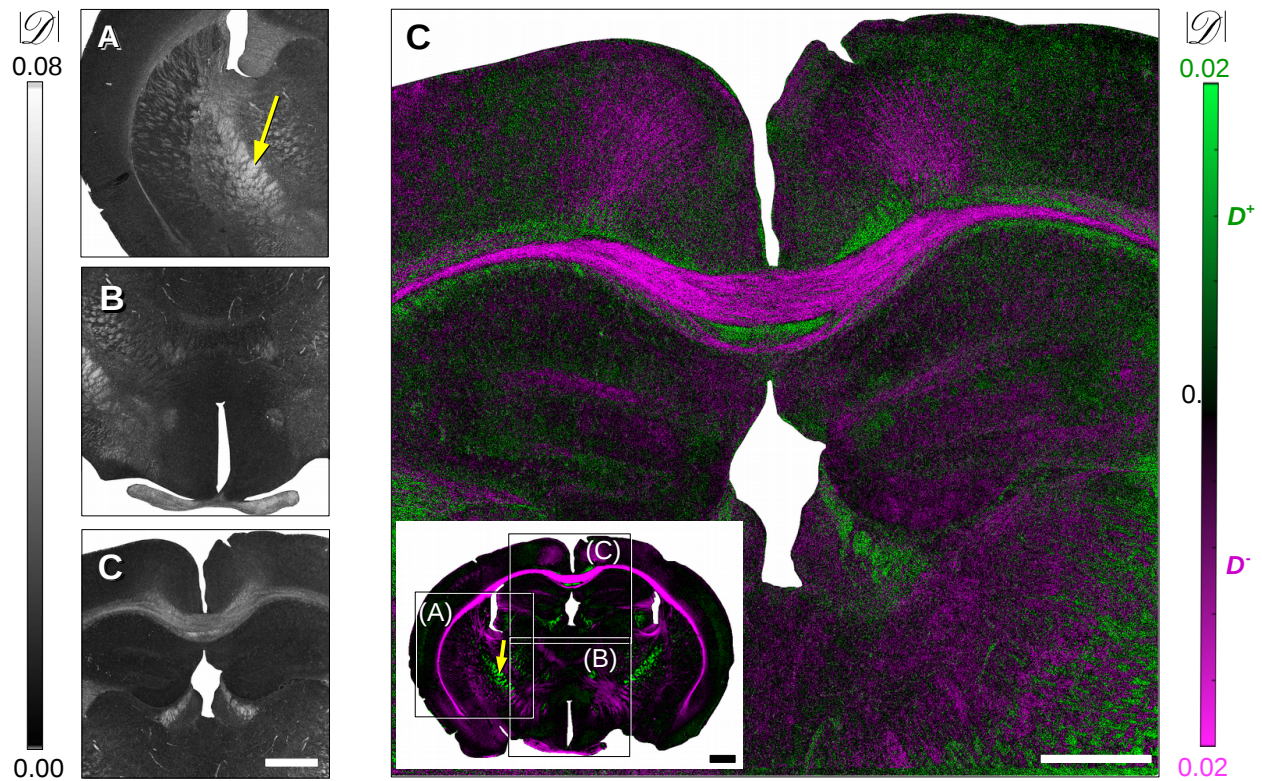


**Fig. 4.** Diattenuation images of a coronal mouse brain section (cf. Fig. 2A) obtained from polarimetric measurements performed with the LAP (whole brain section) and with a prototypic polarizing microscope realized on an optical bench [11] (areas A–C, see *Methods*). The measurement with the LAP was performed with an effective object-space resolution of  $14\ \mu\text{m}/\text{px}$  one day after tissue embedding. The measurements with the polarizing microscope were performed with a pixel size of about  $1.8\ \mu\text{m}$  two days after tissue embedding. The gray-scale images show the strength of the diattenuation signal  $|\mathcal{D}|$ , the colored images show the diattenuation values belonging to regions with diattenuation of type  $D^+$  ( $\varphi_D - \varphi_P \in [-20^\circ, 20^\circ]$ , in green) and regions with diattenuation of type  $D^-$  ( $\varphi_D - \varphi_P \in [70^\circ, 110^\circ]$ , in magenta). The yellow arrows mark the maximum diattenuation measured with the microscope. The diattenuation in a region of  $10 \times 10$  pixels ( $|\mathcal{D}| \approx 9.9\%$ ) is much larger than the diattenuation of the same region measured with the LAP ( $|\mathcal{D}| \approx 3.6\%$ ). However, large diattenuation values and diattenuation of type  $D^+$  or  $D^-$  are observed in similar regions, i. e. the diattenuation effects do not depend on the optical resolution of the imaging system. (Scale bars: 1 mm)

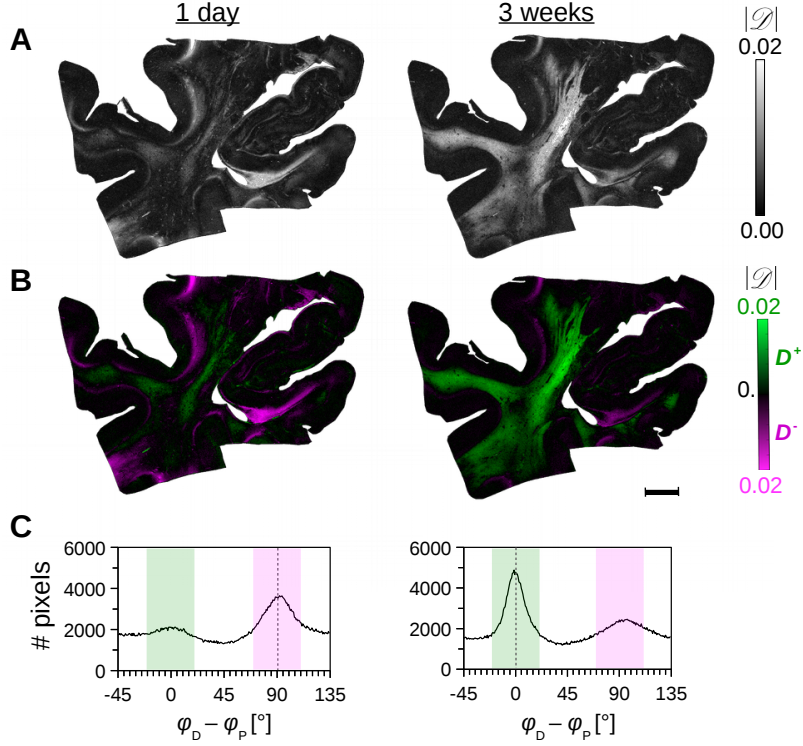


**Fig. 5.** Diattenuation for aging human brain tissue samples (coronal section of human temporal lobe measured one day and three weeks after tissue embedding). (A) Strength of the measured diattenuation signal  $|\mathcal{D}|$ . (B and C) Diattenuation images and  $(\varphi_D - \varphi_P)$  histograms. Diattenuation values that belong to regions with diattenuation of type  $D^+$  ( $\varphi_D - \varphi_P \in [-20^\circ, 20^\circ]$ ) are shown in green, diattenuation values that belong to regions with diattenuation of type  $D^-$  ( $\varphi_D - \varphi_P \in [70^\circ, 110^\circ]$ ) are shown in magenta. The values  $\{|\mathcal{D}|, \varphi_D, \varphi_P\}$  were determined from polarimetric measurements with the LAP (see *Methods*) with an effective object-space resolution of  $40 \mu\text{m}/\text{px}$ . After three weeks, much more regions show diattenuation of type  $D^+$  (green) and the main peak of  $(\varphi_D - \varphi_P)$  is shifted from about  $90^\circ$  to  $0^\circ$ . (Scale bar: 5 mm)

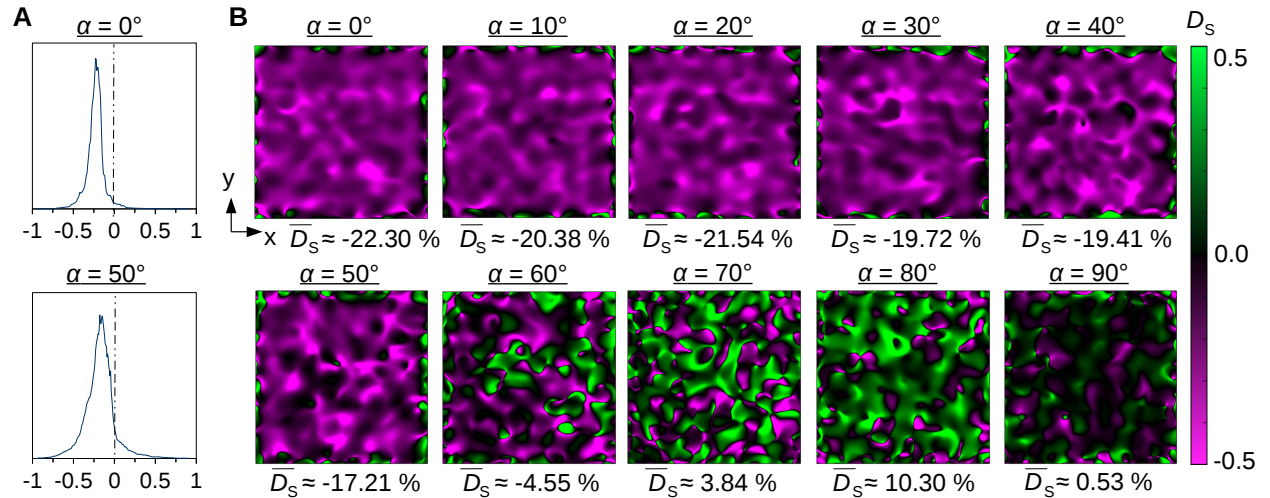


**Fig. 6.** Diattenuation simulated for the bundle of densely grown fibers (see Fig. 3A) for different inclination angles  $\alpha$ . (A) Histograms of  $D_S$  for  $\alpha = 0^\circ$  (mean:  $-22\% \pm 12\%$ ) and  $\alpha = 50^\circ$  (mean:  $-17\% \pm 19\%$ ). (B) Diattenuation images  $D_S$  and mean values  $\overline{D_S}$  for all inclination angles. Positive diattenuation values (representing type  $D^+$ ) are displayed in green, negative diattenuation values (representing type  $D^-$ ) are displayed in magenta. The diattenuation images were obtained from simulated diattenuation measurements with light polarized along the x-axis ( $I_x$ ) and along the y-axis ( $I_y$ ):  $D_S = (I_x - I_y)/(I_x + I_y)$  (see *Methods*). The diattenuation is mostly negative (magenta) for fibers with small inclination angles ( $\alpha \leq 50^\circ$ ) and becomes more positive (green) for steeper fibers ( $\alpha > 60^\circ$ ).

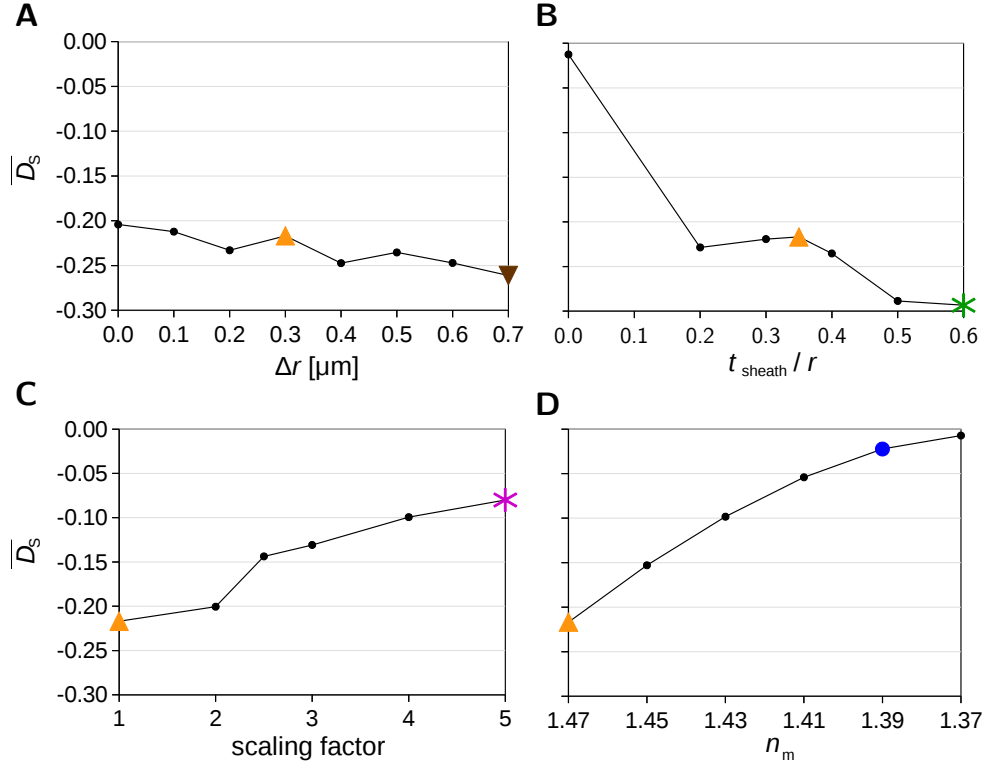


**Fig. 7.** Mean diattenuation values  $\overline{D}_S$  obtained from simulations of the horizontal bundle of densely grown fibers (cf. Fig. 3A with  $\alpha = 0^\circ$ ) for different fiber properties (see *Methods*): (A) different fiber radius distributions  $r \in [r_{\min}, r_{\max}]$  with  $\Delta r \equiv r_{\max} - r_{\min}$  and  $(r_{\max} + r_{\min})/2 = 0.65 \mu\text{m}$ , (B) different myelin sheath thicknesses  $t_{\text{sheath}}$  (relative to the fiber radius  $r$ ), (C) different scaling factors (fiber sizes), (D) different myelin refractive indices  $n_m$ . The values belonging to the graphs in Fig. 3C are highlighted in the respective colors: bundle of densely grown fibers with  $\{r \in [0.5, 0.8] \mu\text{m}, t_{\text{sheath}} = 0.35r, n_m = 1.47\}$  (orange triangle), bundle with broad distribution of radii  $r \in [0.3, 1.0] \mu\text{m}$  (brown triangle), bundle with thick myelin sheaths  $t_{\text{sheath}} = 0.6r$  (green star), bundle with large fibers  $r \in [2.5, 4.0] \mu\text{m}$  (magenta star), bundle with reduced myelin refractive index  $n_m = 1.39$  (blue circle). The mean diattenuation becomes less negative with smaller fiber radius distribution, smaller myelin sheath thickness, larger fiber size (scaling factor), and smaller myelin refractive index.

## Supplementary Note 1. Analytical Model of Dichroism

### Dichroism in Uniaxial Absorbing Materials

In uniaxial absorbing materials with high symmetry, the birefringence (anisotropic refraction) and the dichroism (anisotropic absorption) can be described by a complex retardance with shared principal axes.

Defining a complex refractive index

$$n' \equiv n + i\kappa \equiv n(1 + i\hat{\kappa}) \quad (1)$$

and assuming weak absorption ( $\kappa \ll n$ ), the absorption of the extraordinary light wave ( $\hat{\kappa}_e$ ) is given by (cf. [26], Sec. 15.6.1):

$$v_e^2 \hat{\kappa}_e = v_o^2 \hat{\kappa}_o \cos^2 \theta + v_E^2 \hat{\kappa}_E \sin^2 \theta, \quad (2)$$

where  $\theta$  is the angle between the optic axis (symmetry axis) and the wave vector,  $v$  is the phase velocity of the light, and the indices “o”, “e”, and “E” denote the properties of the ordinary wave (polarized perpendicularly to the optic axis), the extraordinary wave, and the principal extraordinary wave (polarized parallel to the optic axis), respectively.

Writing  $\hat{\kappa} = \kappa/n$ ,  $v = c/n$  ( $c$  is the velocity of light in vacuum), and defining  $\Delta n \equiv n_E - n_o$ ,  $\Delta n_e \equiv n_e - n_o$ ,  $\Delta\kappa \equiv \kappa_E - \kappa_o$ , Eq. (2) yields:

$$\kappa_e = \frac{n_e^3}{n_o^3} \kappa_o \cos^2 \theta + \frac{n_e^3}{n_E^3} \kappa_E \sin^2 \theta \quad (3)$$

$$= \underbrace{\frac{(n_o + \Delta n_e)^3}{n_o^3}}_{f_1(\Delta n_e)} \kappa_o \cos^2 \theta + \underbrace{\frac{(n_o + \Delta n_e)^3}{(n_o + \Delta n)^3}}_{f_2(\Delta n_e, \Delta n)} (\kappa_o + \Delta\kappa) \sin^2 \theta. \quad (4)$$

The birefringence of biological tissue ( $|\Delta n| = 0.001\text{--}0.01$  [27]) is small compared to its refractive index values ( $n = 1.3\text{--}1.5$  [28]). In this case, a first order Taylor expansion (in 2D) can be applied to the functions  $f_1$  and  $f_2$  in  $\{\Delta n_e = 0, \Delta n = 0\}$ :

$$f_1(\Delta n_e) = f(0) + f'(0)\Delta n_e + \dots \quad (5)$$

$$= 1 + \frac{3}{n_o} \Delta n_e + \dots \quad (6)$$

$$f_2(\Delta n_e, \Delta n) = f(0,0) + \frac{\partial}{\partial \Delta n_e} f(0,0)\Delta n_e + \frac{\partial}{\partial \Delta n} f(0,0)\Delta n + \dots \quad (7)$$

$$= 1 + \frac{3}{n_o} (\Delta n_e - \Delta n) + \dots \quad (8)$$

For  $|\Delta n| \ll n$ , the following approximation can be used, see ref. [1] Eq. (A5):

$$\Delta n_e \approx \Delta n \sin^2 \theta. \quad (9)$$

Inserting Eqs. (6) and (8) into Eq. (4) and using Eq. (9) yields:

$$\kappa_e \approx \left(1 + \frac{3}{n_o} \Delta n \sin^2 \theta\right) \kappa_o \cos^2 \theta + \left(1 - \frac{3}{n_o} \Delta n \cos^2 \theta\right) (\kappa_o + \Delta\kappa) \sin^2 \theta \quad (10)$$

$$= \kappa_o + \left(1 - \frac{3}{n_o} \Delta n \cos^2 \theta\right) \Delta\kappa \sin^2 \theta. \quad (11)$$

For  $|\Delta n| \leq 0.01$  and  $n \geq 1.3$ , the term in round brackets in Eq. (11) is  $> 0.97$  and  $\kappa_e \approx \kappa_o + \Delta\kappa \sin^2 \theta$ .

Thus, in uniaxial absorbing materials with small birefringence ( $|\Delta n| \ll n$ ) and weak absorption ( $\kappa \ll n$ ) like brain tissue, the dichroism (anisotropic absorption) depends on the angle  $\theta$  between the wave vector and the optic axis, just like the birefringence in Eq. (9):

$$\Delta\kappa_e \equiv \kappa_e - \kappa_o \approx \Delta\kappa \sin^2 \theta, \quad \Delta\kappa \equiv \kappa_E - \kappa_o. \quad (12)$$

### Inclination Dependence of Dichroism

The diattenuation of a brain section is computed via:

$$D = \frac{I_{\parallel} - I_{\perp}}{I_{\parallel} + I_{\perp}}, \quad (13)$$

with  $I_{\parallel}$  and  $I_{\perp}$  being the (maximum and minimum) transmitted light intensities for light polarized parallel and perpendicularly to the projection of the optic axis (predominant orientation of the nerve fibers) onto the section plane.

For light propagating through a brain section of thickness  $d$ , the transmitted light intensity is given by the Beer-Lambert law:

$$I = I_0 e^{-\mu d}, \quad (14)$$

where  $I_0$  is the ingoing light intensity and  $\mu$  the attenuation coefficient of the material which depends on the direction of polarization. With this definition, Eq. (13) can be written as:

$$D = \frac{e^{-d\mu_{\parallel}} - e^{-d\mu_{\perp}}}{e^{-d\mu_{\parallel}} + e^{-d\mu_{\perp}}} = \frac{e^{d(\mu_{\perp} - \mu_{\parallel})/2} - e^{-d(\mu_{\perp} - \mu_{\parallel})/2}}{e^{d(\mu_{\perp} - \mu_{\parallel})/2} + e^{-d(\mu_{\perp} - \mu_{\parallel})/2}} \quad (15)$$

$$= \tanh\left(d \frac{\mu_{\perp} - \mu_{\parallel}}{2}\right). \quad (16)$$

To estimate how the dichroism of brain tissue depends on the nerve fiber inclination, we assume that the diattenuation is solely caused by anisotropic absorption, neglecting any scattering. In this case, the attenuation coefficient is given by the absorption coefficient ([29] p. 227):

$$\mu = K \equiv \frac{4\pi\kappa}{\lambda}, \quad (17)$$

where  $\kappa$  is the imaginary part of the refractive index in the medium (see Eq. (1)) and  $\lambda$  the wavelength of the light. In a similar way, we define the absorption coefficient of the ordinary wave ( $K_{\perp} \equiv 4\pi\kappa_o/\lambda$ ) and of the extraordinary wave ( $K_{\parallel} \equiv 4\pi\kappa_e/\lambda$ ), taking into account that the ordinary wave is polarized perpendicularly to the optic axis while the extraordinary wave is polarized parallel to the projection of the optic axis onto the section plane.

With these definitions, the diattenuation caused by anisotropic absorption (dichroism) can be written as:

$$D_K \stackrel{(16)}{=} \tanh\left(\frac{d}{2}(K_{\perp} - K_{\parallel})\right) \stackrel{(17)}{=} \tanh\left(\frac{2\pi d}{\lambda}(\kappa_o - \kappa_e)\right) \stackrel{(12)}{\approx} \tanh\left(-\frac{2\pi d}{\lambda} \Delta\kappa \sin^2 \theta\right), \quad (18)$$

where  $\theta$  is the angle between the optic axis (nerve fiber orientation) and the wave vector (direction of propagation).

Assuming that the brain section is illuminated under normal incidence, the out-of-plane inclination angle of the fibers is given by:  $\alpha = 90^\circ - \theta$ . Thus, the dichroism of brain tissue decreases with increasing fiber inclination angle and does not change its sign (cf. Fig. 3C):

$$D_K \approx \tanh\left(-\frac{2\pi d}{\lambda} \Delta\kappa \cos^2 \alpha\right). \quad (19)$$

Freshly embedded brain sections show diattenuation of both types  $D^+$  and  $D^-$  (see Fig. 2). This suggests that the diattenuation is not only caused by dichroism (anisotropic absorption) but also by anisotropic scattering of light. With increasing time after tissue embedding, the scattering is expected to decrease due to an equalization of the refractive indices. Thus, the diattenuation of type  $D^+$  that is observed in brain sections with long embedding time (see Figs. 1 and 5) is presumably caused by dichroism, i. e.  $D_K > 0 \Leftrightarrow I_{\parallel} > I_{\perp}$ . This means that the absorption becomes maximal (the transmitted light intensity becomes minimal) when the light is polarized perpendicularly to the fiber axis, i. e. in the plane of the radially oriented lipid molecules in the myelin sheaths. This suggests that dichroism of brain tissue is mainly caused by the myelin lipids and is therefore not expected to change with increasing time after tissue embedding.